ADVANCED MATERIALS
www.advmat.de

Coordination Polymer to Atomically Thin, Holey, Metal-Oxide Nanosheets for Tuning Band Alignment

Sajjad S. Mofarah, Esmaeil Adabifiroozjaei,* Raheleh Pardehkhorram, M. Hussein N. Assadi, Manuel Hinterstein, Yin Yao, Xinhong Liu, Mohammad B. Ghasemian, Kourosh Kalantar-Zadeh, Rashid Mehmood, Claudio Cazorla, Reza Shahmiri, Ghazaleh Bahmanrokh, Saroj Bhattacharyya, Maria Chiara Spadaro, Jordi Arbiol, Sean Lim, Yuwen Xu, Hamidreza Arandiyan, Jason Scott, Pramod Koshy,* and Charles C. Sorrell*

Holey 2D metal oxides have shown great promise as functional materials for energy storage and catalysts. Despite impressive performance, their processing is challenged by the requirement of templates plus capping agents or high temperatures; these materials also exhibit excessive thicknesses and low yields. The present work reports a metal-based coordination polymer (MCP) strategy to synthesize polycrystalline, holey, metal oxide (MO) nanosheets with thicknesses as low as two-unit cells. The process involves rapid exfoliation of bulk-layered, MCPs (Ce-, Ti-, Zr-based) into atomically thin MCPs at room temperature, followed by transformation into holey 2D MOs upon the removal of organic linkers in aqueous solution. Further, this work represents an extra step for decorating the holey nanosheets using precursors of transition metals to engineer their band alignments, establishing a route to optimize their photocatalysis. The work introduces a simple, high-yield, room-temperature, and template-free approach to synthesize ultrathin holey nanosheets with high-level functionalities.

State-of-the-art holey 2D structures have established new levels of functionalities for materials, particularly for energy and environmental applications.[1,2] The formation of holes in nanosheets enhances the density of accessible active sites and rapid lateral charge carrier diffusion.[3] However, to minimize the transverse diffusion distances within holey 2D materials, sheets of atomic thickness should be achieved. Additionally, to retain highly active sheets, polycrystalline 2D planar materials are desirable to prevent irreversible restacking of the nanosheets. Although there are some reports on synthesis of ultrathin polycrystalline nanosheets,[4] the synthesis of polycrystalline holey 2D sheets by either top-down or bottom up strategies has remained elusive for most compounds.

Holey 2D graphene[5] and holey 2D transition metal chalcogenides (TMCs) and selenides (TMS) have been reported.[6,7] However, the processing is relatively complex, including the requirement of surfactants, sacrificial templates, and/or additional steps for removal of the template at high temperatures; these ultimately

Dr. S. S. Mofarah, Dr. M. H. N. Assadi, Dr. M. Hinterstein, X. Liu, Dr. R. Mehmood, Dr. C. Cazorla, R. Shahmiri, Dr. G. Bahmanrokh, Y. Xu, Dr. P. Koshy, Prof. C. C. Sorrell
School of Materials Science & Engineering
UNSW Sydney
Sydney, NSW 2052, Australia
E-mail: s.seifimofarah@unsw.edu.au; koshy@unsw.edu.au

Dr. E. Adabifiroozjaei
Research Center for Functional Materials (RCFM)
National Institute for Materials Science (NIMS)
Tsukuba, Ibaraki 305-0047, Japan
E-mail: adabifiroozjaei.e@nims.go.jp

Dr. R. Pardehkhorram
School of Chemistry
UNSW Sydney
Sydney, NSW 2052, Australia

The ORCID identification number(s) for the author(s) of this article can be found under https://doi.org/10.1002/adma.201905288.

Dr. M. H. N. Assadi
Center for Green Research on Energy and Environmental Materials (GREEN)
National Institute for Materials Science (NIMS)
Tsukuba, Ibaraki 305-0044, Japan

Dr. M. Hinterstein
Institute for Applied Materials
Karlsruhe Institute of Technology
76131 Karlsruhe, Germany

Dr. Y. Yao, S. Lim
Electron Microscopy Unit (EMU)
Mark Wainwright Analytical Centre
UNSW Sydney
Sydney, NSW 2052, Australia

Dr. M. B. Ghasemian, Prof. K. Kalantar-Zadeh
School of Chemical Engineering
UNSW Sydney
Sydney, NSW 2052, Australia

DOI: 10.1002/adma.201905288

result in nanosheet thicknesses of tens of nanometers.[8] Demonstration of effective synthesis of holey 2D metal oxides (MOs) is an important yet unrealized aim for their incorporation in efficient energy and catalytic systems.

The present work demonstrates an alternative, simple, and adaptable strategy to create polycrystalline holey 2D nanostructures of MOs at room temperature without the use of a template. This unique technique is based on the rapid exfoliation of bulk-layered, metal-based coordination polymers (MCPs) into monolayers in aqueous solutions, followed by transformation into holey 2D MOs as thin as two-unit cell thickness (for instance, ≈1.1 nm for CeO_2 and ZrO_2) but lateral sizes in the millimeter scale (≈5 mm). In this process, a suspension of an unstable metal hydroxide substructure that is symmetrically capped by a bidentate organic ligand is exposed to an increase in pH, which results in the removal of the organic linkers and enables subsequent formation of the holey MO nanosheets. Further, as a proof of this versatile concept, holey 2D nanostructures of TiO_2 and ZrO_2 were synthesized using the corresponding MCPs as precursor. Additionally, the broad applicability of this strategy is illustrated through the synthesis of mixed 0D/2D heterostructures of 0D transition metal oxides (TMOs) onto 2D CeO_{2-x} templates. The decoration of the 2D CeO_{2-x} nanostructures with the 0D TMOs resulted in rearrangements of the band alignments and thus modification of the electronic properties. First-principle calculations based on density functional theory (DFT) confirm the band structure differences observed for CeO_2 nanosheets, bulk CeO_2, and 0D/2D heterostructures. The holey CeO_{2-x}-based nanosheets show strong photocatalytic activity under simulated solar light.

The cerium-based coordination polymer (Ce-CP) was synthesized by modified anodic electrochemical deposition. **Figure 1**a shows scanning electron microscopy (SEM) image of a freestanding Ce-CP hexagonal tube with bulk-layered structure. Additionally, transmission electron microscopy (TEM) image and the corresponding schematic are shown in Figure 1b,c, respectively. The details of the Ce-CP formation mechanism are provided in Figures S1–S3 (Supporting Information). The stratified Ce-CP tube can be readily exfoliated, upon ultrasonication in deionized (DI) water at room temperature. Figure 1d,e shows ex situ SEM and TEM images of the Ce-CP partly exfoliated after 4 min of ultrasonication. The corresponding schematic is shown in Figure 1f. Longer sonication treatment (8 min) led to the complete Ce-CP exfoliation, as illustrated by SEM and TEM images in Figure 1g,h, respectively. The total exfoliation progress as a function of sonication time is schematically demonstrated in Figure 1c–i. The final step involves increasing the pH of the solution to pH = 8, during ultrasonication, leading to the transformation of the Ce-CP nanosheets into defective CeO_{2-x} nanosheets. It is significant to note that, during this transformation, high densities of nanoholes across the ultrathin sheets are formed as shown in Figure 1j,k. This is attributed to the rapid removal of the organic bidentate trichloroacetate (TCA) linkers, owing to high field strength of Ce(IV) over a wide pH range and thus a corresponding strong affinity for CeO_{2-x} formation.[9] The schematic of the holey structure of the CeO_{2-x} nanosheet is also shown in Figure 1l.

Owing to the absence of reference data consistent with the X-ray diffraction (XRD) pattern obtained for the Ce-CP, the corresponding crystal structure was investigated by comparative ab initio molecular dynamics simulations and XRD and neutron diffraction patterns, as provided in Figures S4–S17 and Tables S1–S5 (Supporting Information). The data describing the crystallography of the Ce-CP, which has been determined to be $Ce(TCA)_2(OH)_2\cdot 2H_2O$, was indexed to be triclinic system, space group $P\bar{1}$, with $a = 1.31$ nm, $b = 1.32$ nm, $c = 1.10$ nm, $\alpha = 81.20°$, $\beta = 93.21°$, and $\gamma = 112.93°$.

The crystal structure of the stratified Ce-CP is illustrated in Figure 1m, where the interlayer spaces are mutually held together by intercalated protons and the terminating chlorine ions of the TCA ligands. The application of ultrasonication on the Ce-CP tubes enhances the exfoliation through the vibration's breakage of the nanosheet and resultant facilitated water molecule penetration (Figure 1n). Further, the *c*-axis lattice parameter of the Ce-CP crystal structure was measured to be 1.1 nm (see Table S5 in the Supporting Information), which represents the thinnest possible Ce-CP nanosheet of a Ce-CP monolayer. Increasing the pH of the solution, leads to dissolution of the TCA from the two surfaces (Figure 1n) of the M-OH substructure. This is followed by conversion of a highly reactive interior M-OH ($Ce(OH)_2^{2+}$) substructure to the more stable $Ce(OH)_4$ followed by the rapid formation of stable CeO_{2-x} (Figure 1o) without any morphological changes. The structural evolution during the Ce-CP transformation into CeO_{2-x} are studied using XRD and selected-area diffraction pattern (SAED) analysis (Figure S18, Supporting Information). In order to confirm the removal of the TCA, energy dispersive spectroscopy (EDS) elemental mapping was carried out for both Ce-CP and CeO_{2-x} nanosheets, as shown in Figures S19 and S20 (Supporting Information), respectively. Furthermore, the rapid evolution of Ce-CP into CeO_{2-x} is studied by in situ laser Raman microspectroscopy of nanosheets subjected to an alternative removal method (Figure S21, Supporting Information).

The holey architecture of the CeO_{2-x} nanosheet was explored using high-angle annular dark-field (HAADF) TEM images as shown in **Figure 2**a–c, where single crystallites of lateral sizes in

Dr. R. Mehmood
Department of Physics and Astronomy
ARC Centre of Excellence for Nanoscale BioPhotonics
Macquarie University
Sydney, NSW 2109, Australia
Dr. S. Bhattacharyya
Mark Wainwright Analytical Centre
UNSW Sydney
Sydney, NSW 2052, Australia
Dr. M. C. Spadaro, Prof. J. Arbiol
Catalan Institute of Nanoscience and Nanotechnology (ICN2)
CSIC and BIST
Campus UAB
Bellaterra, 08193 Barcelona, Catalonia, Spain
Prof. J. Arbiol
Catalan Institution for Research and Advanced Studies (ICREA)
Pg. Lluís Companys 23, 08010 Barcelona, Catalonia, Spain
Dr. H. Arandiyan
Laboratory of Advanced Catalysis for Sustainability
School of Chemistry
University of Sydney
Sydney, NSW 2006, Australia
Dr. J. Scott
Particles and Catalysis Research Group
School of Chemical Engineering
UNSW Sydney
Sydney, NSW 2052, Australia

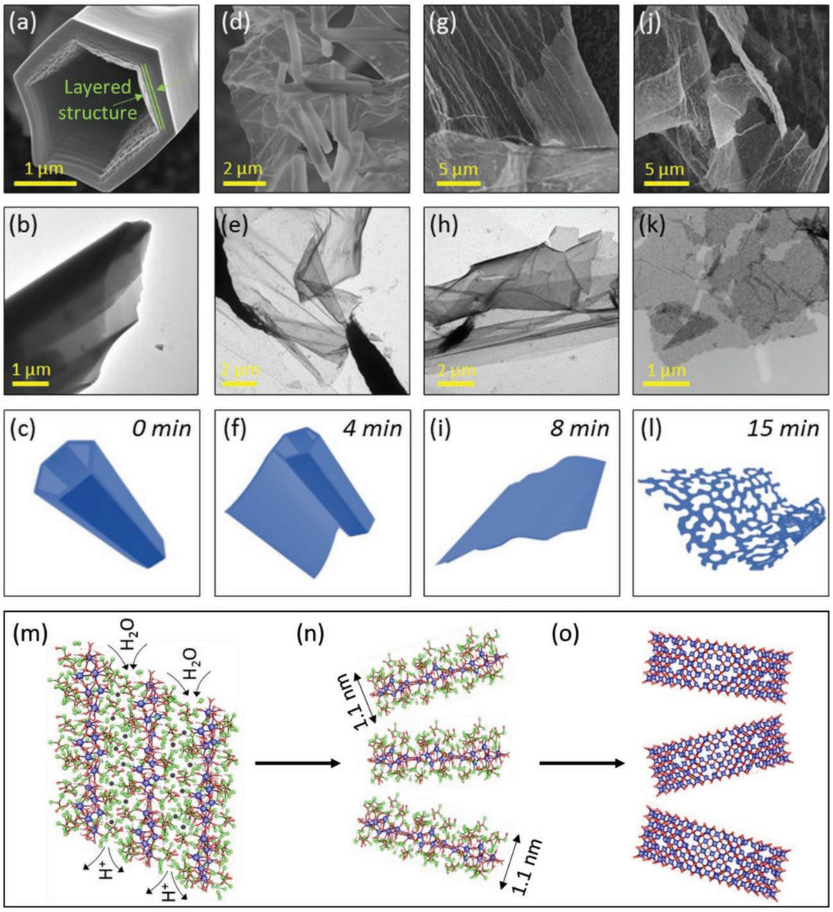

Figure 1. Exfoliation and conversion of Ce-CP nanotube into holey 2D CeO_{2-x} structures. a–c) Ex situ SEM, TEM, schematic of Ce-CP hexagonal. d–f) Ex situ SEM, TEM, schematic of Ce-CP nanosheet obtained by exfoliation of the Ce-CP hexagonal nanotube for 4 min at room temperature. g–i) Ex situ SEM, TEM, schematic of Ce-CP nanosheet obtained by exfoliation of the Ce-CP hexagonal nanotube for 8 min at room temperature. j–l) Ex situ SEM, TEM, schematic of holey CeO_{2-x} nanosheet obtained by exfoliation of the Ce-CP hexagonal nanotube for 15 min at room temperature in basic aqueous solution (pH = 8). m) Schematic of layered structure of Ce-CP, n) Ce-CP exfoliated nanosheets as a result of penetration of water molecules between stacked Ce-CP nanosheets, o) highly defective CeO_{2-x} nanosheets. Blue, green, red, brown, and black spheres represent cerium, chlorine, oxygen, carbon, and hydrogen ions, respectively. Gaps within the defective CeO_{2-x} nanosheet represent oxygen vacancies.

the range 3–6 nm intersect to create nanoholes at the multiple grain boundary junctions owing to imperfect nanosheet packing. Similar to the work of Peng et al.,[8c] the conclusion of strong chemical bonding between the crystallites is supported by the apparent intergrowths at the grain boundaries, despite their high angles, as suggested by merged lattice fringes (Figure S22, Supporting Information). Further, the high structural and morphological stabilities of the nanosheet were shown by TEM and Raman results (Figure S23, Supporting Information). The constraint of the crystallites to 2D is important because this facilitates perfect lattice correspondence by symmetric atomic registry of the cubic oxide lattices across the interface, regardless of grain boundary angle. This unusual condition enables the self-assembly of large, ultrathin, polycrystalline MCP nanosheets, regardless of orientation, where the M-OH substructures, act as nodes, attain atomic registry and the organic linkers contribute to bridging the nodes. However, as the individual nanosheets have irregular outlines, nanoholes are formed when atomic registry is not possible. The creation of holes introduces new exposed surfaces that improves charge carrier transportation and also generate defects at the edge surfaces. In order to highlight the superior properties of the holey 2D nanosheets, in comparison with 0D nanoparticles, number of physical and defect characterization tests were carried out, the results of which are illustrated in Figure S24 (Supporting Information). Although X-ray photoelectron spectroscopy (XPS) results obtained from 0D and 2D structures show high $[V_O^{\bullet\bullet}]$ for both 0D and 2D CeO_2 nanostructures (Figure S25, Supporting Information), the electron paramagnetic resonance (EPR) spectra for the former showed broad and relatively low intensity signal suggesting limited density of accessible defects. This can be attributed to the nature of aggregated 0D nanoparticles, as shown by TEM images in Figure S26 (Supporting Information), where single crystallites in the range 3–6 nm are strongly bonded as shown by the lattice fringes of adjacent grains. In contrast, the holey 2D nanostructure exhibited high EPR spectra intensity, which can be attributed to the great number of accessible defects, owing to the high exposed surface area. The efficiency of the defects is also studied by photoluminescence (PL) test as shown in Figure S27 (Supporting Information), where the intensity of the spectra is considered to be representative of the density (extent) of electron/hole recombination. The PL spectra corresponding to the 0D structure illustrates high intensity (high recombination rate), relative to the 2D structure.

A high density of defects in the CeO_{2-x} nanosheets is also illustrated by electron energy loss spectroscopy (EELS), as shown in Figure 2d,e. The EELS data show that $V_O^{\bullet\bullet}$ are present both on the grain boundaries (Figure 2d) and within the CeO_{2-x} crystallites (Figure 2e). The intensity ratio of the M_5 (3d 5/2 → 4f 7/2) and M_4 (3d 3/2 → 4f 5/2) peaks are known to show a linear relationship, where the higher ratio indicates higher $[V_O^{\bullet\bullet}]$.[10] The EELS data allow the determination of the $[V_O^{\bullet\bullet}]$ from the ratio of the M_5 (orange) and M_4 (green) peaks, where the ratios for minimal $[V_O^{\bullet\bullet}]$ (0 at% for stoichiometric $CeO_{2.0}$) and maximal $[V_O^{\bullet\bullet}]$ (25 at% for $CeO_{1.5}$) are ≈0.9 and ≈1.25, respectively. The EELS data indicate a $[V_O^{\bullet\bullet}]$ of 0.95 within the crystallite and 1.15 at the interface of two crystallites. While the higher $[V_O^{\bullet\bullet}]$ at the crystallite interface and surfaces are as expected,[11,12] the presence of $V_O^{\bullet\bullet}$ within the crystallite has been recently reported.[9b] The formation of such defects is likely to result from the low energy required to transform Ce-CP into CeO_{2-x} in aqueous solution at room temperature and the consequent imperfect recrystallization.

It is notable that the high-magnification HAADF image of the holey nanosheet (Figure 2f) indicates the presence of Ce vacancies (V_{Ce}''''), which to the best of our knowledge do not appear to have been reported for CeO_2-based materials. This

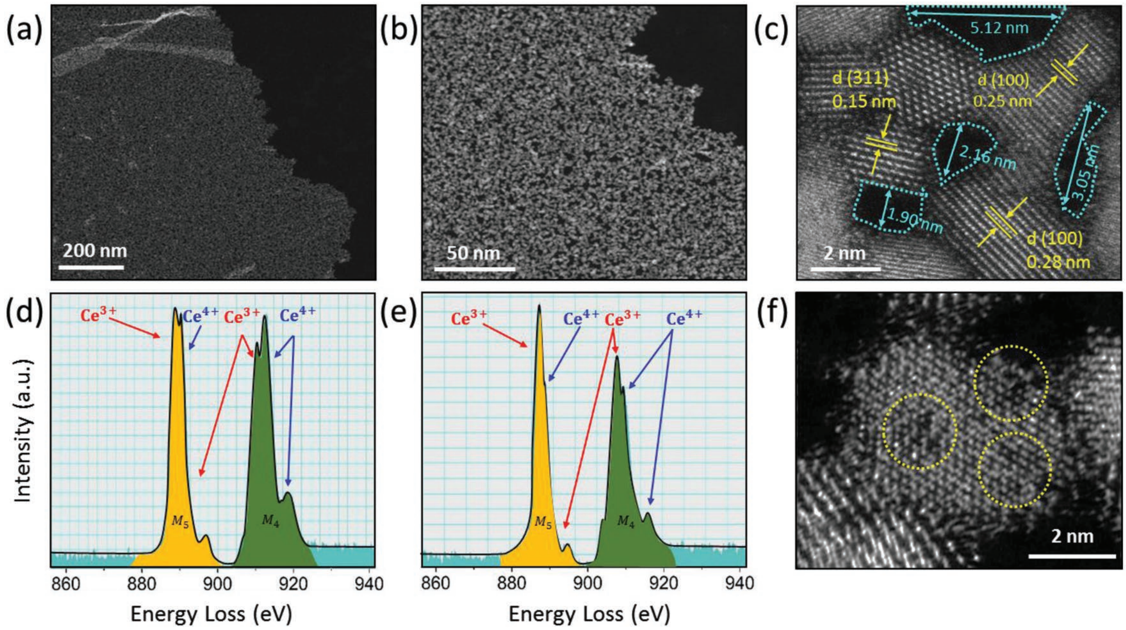

Figure 2. Defect and structural analysis of CeO_{2-x} holey nanosheets. a,b) Low-magnification HAADF image of CeO_{2-x} nanosheets. c) High-magnification HAADF image of CeO_{2-x} nanosheets illustrating nanoholes of ≈2–5 nm lateral size. d) EELS spectra from an intercrystallite region in CeO_{2-x} nanosheets. e) EELS spectra from within a CeO_{2-x} crystallite. f) High-magnification HAADF image showing Ce vacancies within a CeO_{2-x} crystallite.

defect may indicate Schottky pair formation, which requires ≈2–3 eV more than that required for O vacancy formation.[13] Nonetheless, this may be compensated by the short diffusion distances (lateral and transverse) in the nanosheets. Both the HAADF imaging and EELS analysis in STEM mode were conducted while the samples were cooled in situ to liquid nitrogen temperature in order to avoid the creation of artefact vacancies from the high vacuum and/or electron beam irradiation.[14]

The use of Ce-CP as sole precursor in the absence of a template, surfactant, etching or other technical complexities to synthesize holey CeO_{2-x} nanosheets represents a simplified fabrication approach requiring effectively only an electrochemical setup. Critically, the high yield of the process is demonstrated by the synthesis of large amounts of holey CeO_{2-x} nanosheets in a single batch, as shown in Figure S28 (Supporting Information), in which the lateral size of the nanosheets, which are reversibly stacked by van der Waals (vdW) forces, is as large as 5 mm.

Further, the flexibility of the fabrication method is confirmed by the syntheses of a layered titanium-based CP (Ti-CP) and a zirconium-based CP (Zr-CP). Details of the morphological and structural characterization of these bulk layered MCPs are given in Figures S29–S34 (Supporting Information). Similar to Ce-CP, the Ti-CP and Zr-CP were exfoliated rapidly in basic aqueous solutions into nanosheets, as illustrated by TEM and EDS analyses (Figures S35–S47, Supporting Information). The morphological analyses of CeO_{2-x}, TiO_{2-x}, and ZrO_{2-x} nanosheets are shown in **Figure 3**a–c, respectively, where TEM images reveal the holey nanostructures of the MCP-derived MOs. Also, Figure 3d–f shows SAED patterns of the randomly oriented polycrystalline nanosheets indexed to CeO_2, TiO_2, and ZrO_2, respectively. Considering the ultrathin nature of the holey nanosheets, surface chemical analysis effectively provides bulk analysis since the penetration depth of XPS is ≈3 nm.[15] As an example, quantitative analysis of CeO_{2-x} (Figure S48, Supporting Information) was carried out by deconvolution of Ce 3d orbital of XPS spectra revealing significant Ce^{3+} concentrations, which generally are associated with corresponding oxygen vacancy concentrations ($[V_O^{\bullet\bullet}]$) through charge compensation.[16] These results are in agreement with the EELS data shown in Figure 2d,e.

In order to measure the thicknesses of the holey MO nanosheets, atomic force microscopy (AFM) imaging was obtained by the deposition of the nanosheets onto silicon substrates, as shown in Figure 3g–i. The corresponding height-profiles are shown by the two step-heights from the substrate in Figure 3j–l. For CeO_{2-x}, these are ≈1.1 and ≈1.6 nm, indicating that the nanosheets are of two (and three) unit-cell thickness (CeO_2 unit cell = 0.54 nm).[17] The thicknesses of the TiO_{2-x} and ZrO_{2-x} nanosheets also were observed in integral multiples of nanosheet layers of minimal thicknesses of 5 and 3 unit cells, respectively (Table S6, Supporting Information). The slightly larger thickness of the TiO_{2-x} nanosheet is likely to be due to the poor packing arising from the anisotropy of the tetragonal anatase[18] and not because of the introduced process, while the thinner CeO_{2-x} and ZrO_{2-x} nanosheets probably resulted from the effectively equiaxed lattices.[19] These data suggest that self-assembled MOs of equiaxed or possibly highly anisotropic and hence self-aligned nanostructures are more likely to yield thinner nanosheets. According to Zhao et al.,[20] control over the morphological and structural parameters in 2D materials can have a great impact in their properties. Hence, MO nanosheets of variable characteristics can be obtained by regulating the experimental conditions of the fabrication process, as shown by the effects of pH on the pore size (Figure S49, Supporting Information) and of temperature on the thickness (Figure S50, Supporting Information). The details

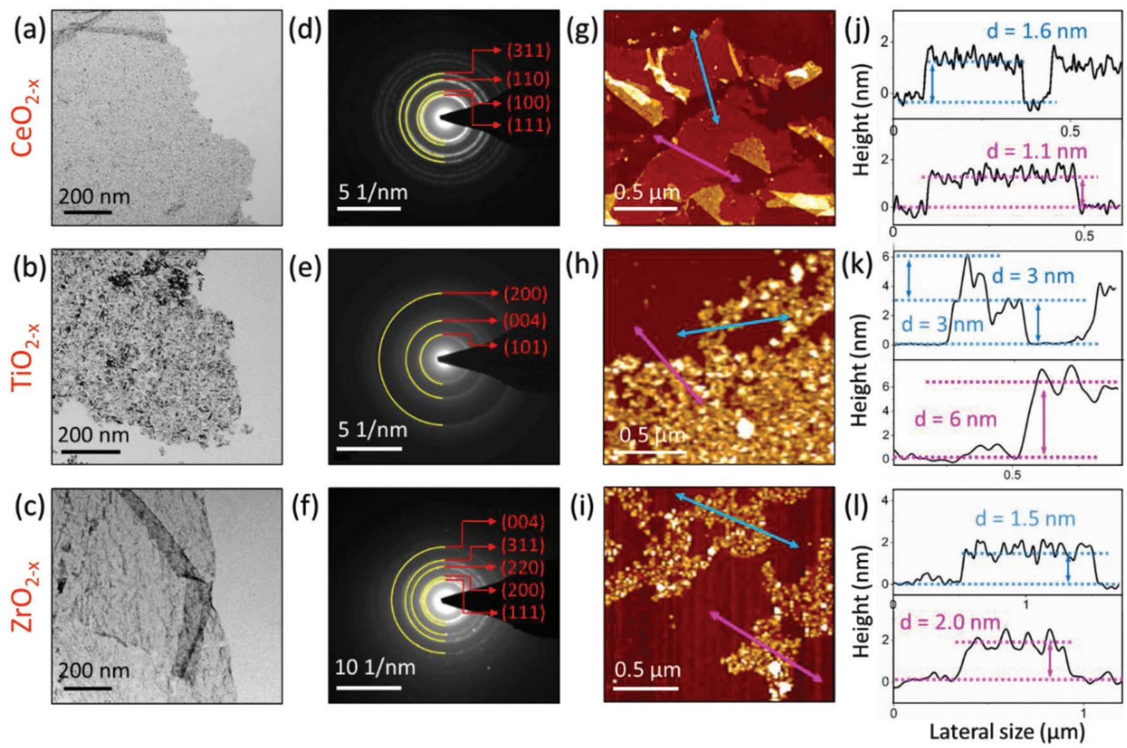

Figure 3. Characterization of holey MO nanosheets. a–c) TEM images for: a) CeO_{2-x} nanosheet, b) TiO_{2-x} nanosheet, and c) ZrO_{2-x} nanosheet. d–f) Corresponding SAED patterns of: d) CeO_{2-x} nanosheet, e) TiO_{2-x} nanosheet, and f) ZrO_{2-x} nanosheet. g–i) AFM images of: g) CeO_{2-x} nanosheet, h) TiO_{2-x} nanosheet, and i) ZrO_{2-x} nanosheet. j–l) Corresponding height profiles for: j) CeO_{2-x} nanosheet, k) TiO_{2-x} nanosheet, and l) ZrO_{2-x} nanosheet.

for physical properties of the holey MO nanosheets, including Brunauer–Emmett–Teller (BET) surface area and pore size, are provided in Table S7 in the Supporting Information. Also, distributions of the pores across the MO nanosheets are shown in Figure S51 in the Supporting Information.

The applicability for holey CeO_{2-x} nanosheets can be broadened by their use as a template in fabrication of mixed 0D/2D heterostructures of FeO_x-decorated CeO_{2-x} (FCO), NiO-decorated CeO_{2-x} (NCO), and ZnO-decorated CeO_{2-x} (ZCO). Using the general synthesis platform, the holey CeO_{2-x} nanosheets were dispersed in an aqueous solution (pH = 6), which yielded a relatively stable suspension with zeta potential of −25 mV (Figure S52, Supporting Information), which is slightly lower than the threshold of −30 mV[21] for fully stable colloidal system. In addition, considering the speciation diagrams for the transition metal ions (Figure S53, Supporting Information), the predominant species, within the acidic pH of CeO_{2-x} suspension, are expected to be TM^{n+}. Therefore, this situation establishes electrostatic attraction between the positively charged metal species and the negatively charged holey nanosheets, thereby providing the mechanism for the assembly of metal species on the nanosheet surfaces.[22] This is confirmed by reductions in the zeta potential for the Fe, Ni, and Zn nanostructure suspensions, respectively. This approach can significantly increase the functionalities of the nanosheets by preventing the layers from stacking during minimization of the interplanar vdW interactions and by maximizing the accessibility of the active sites.[23] Moreover, the mixed 0D/2D heterostructures can provide sufficient hybridization between the atomic orbitals, resulting in enhanced carrier delocalization at the junction interfaces.[23] The elemental, mineralogical, and crystallographic investigations of the nanostructures were carried out by EDS, laser Raman microspectroscopy, and XRD as shown in **Figure 4**. The formation of the nanostructures were shown by EDS mapping of the nanosheets in Figure 4a–c revealing a homogenous distribution of 0D TMOs. Further, the coexistence of the TMOs and CeO_{2-x} was confirmed by the laser Raman microspectra (Figure 4d–f). Since the peak for pristine CeO_2 is at 464 cm^{-1}, the large peaks at ≈460 cm^{-1} for FCO, NCO, and ZCO (assigned to the F_{2g} vibrational mode for the symmetrical stretching of Ce(IV) and eight surrounding oxygens) indicate red shifts to lower wavenumber consistent with expansive strains arising from $V_O^{\bullet\bullet}$. Further, the peak positioned at ≈600 cm^{-1} is attributed to the defect induced mode originating from $V_O^{\bullet\bullet}$, as reported previously.[24] The peaks at 230 cm^{-1} in Figure 4d is assigned to the A_{1g} vibrational mode of α-Fe_2O_3, while the peaks at 294, 395, and 620 cm^{-1} correspond to E_g vibrational modes of α-Fe_2O_3.[25] In addition, there are three deconvoluted peaks at 310 (T_{2g}), 538 (T_{2g}), and 680 (A_{1g}) that can be attributed to the vibrational mode of Fe_3O_4.[24,25] Figure 4e illustrates the coexistence of NiO (magenta color peaks) and CeO_2 (gray peaks). The peaks for E_g, one-phonon transverse optical (1T), one-phonon longitudinal optical (1L), and two-phonon transverse optical (2T) vibrational modes of NiO are laid at 287, 380, 560, and 690 cm^{-1}.[26] Deconvolution of the ZCO peaks in Figure 4f reveals two peaks at 380 and 412 cm^{-1}, which are ascribed to the A_{1T} and E_{1T} vibrational modes of ZnO. Further, the peak at 580 cm^{-1} is assigned to the E_{1L} vibrational mode of ZnO.[27] Similarly, the coexistence

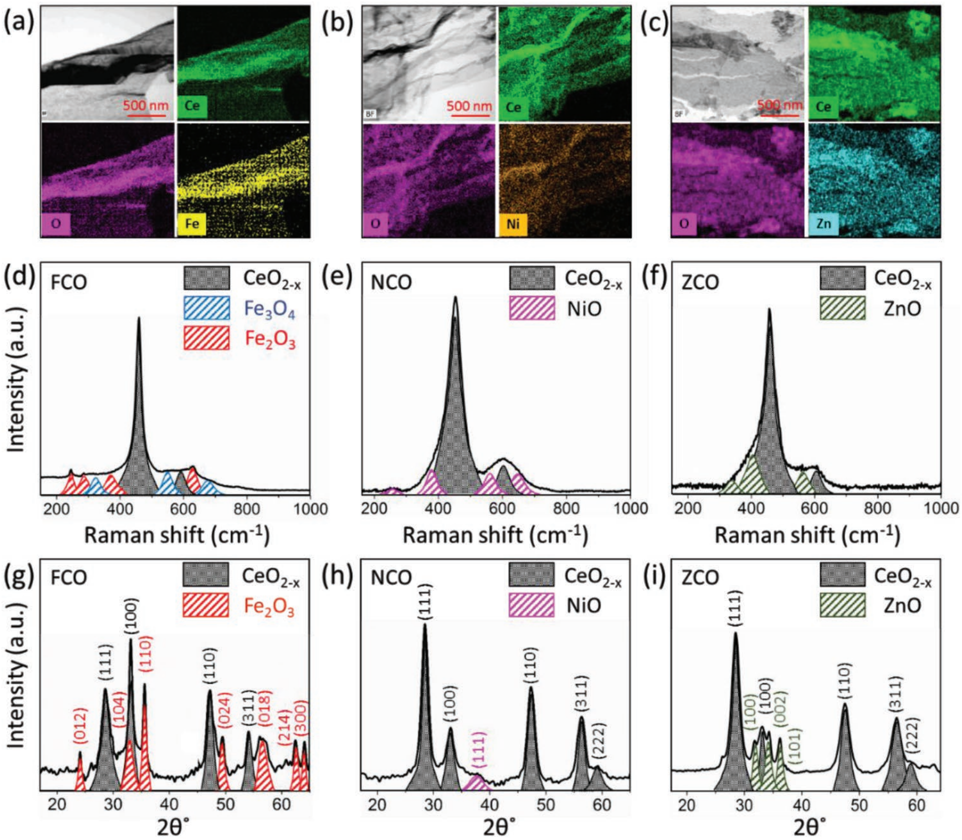

Figure 4. Characterization of TMO in 0D/2D heterostructures. a–c) EDS mapping of FCO, NCO, and ZCO 0D/2D heterostructures, respectively. d–f) Laser Raman microspectra of FCO, NCO, and ZCO 0D/2D heterostructures, respectively. g–i) XRD patterns of FCO, NCO, and ZCO 0D/2D heterostructures, respectively.

of TMOs and CeO_{2-x} nanosheets were confirmed by XRD analysis as shown in Figure 4g–i. Additional data analysis of the nanostructures are provided in Figure S54 (Supporting Information).

In order to investigate the photocatalysis parameters of CeO_{2-x} and the mixed nanostructures, the corresponding electronic band structures were constructed. Hence XPS, UV–vis spectrophotometry, and amplitude-modulated Kelvin probe force microscopy (AM-KPFM) were used to determine the gaps between the valence bands (VB, orange lines) and the Fermi levels (E_f, black dashed lines), optical indirect bandgaps (E_g), and the work functions (Φ). The AFM image in **Figure 5**a illustrates the basis for the KPFM result for CeO_{2-x} shown in Figure 5b. There is a significant difference of 90 mV (0.09 eV) potential between that of the silicon substrate (higher potential) and the deposited 1.2 nm thickness CeO_{2-x} nanosheet (lower potential). Since the Φ of a platinum/iridium-coated silicon tip was measured to be 4.74 eV (similar to that reported previously), then subtracting 0.09 eV gives a Φ for CeO_{2-x} of 4.65 eV.[28] The XPS plot for the valence band of CeO_{2-x} is shown in Figure 5c, where the presence of trapping states within the bandgap is also illustrated. Additionally, the Tauc plot for the E_g is shown in Figure 5d. These data and those for FCO, NCO, and ZCO (Figures S55 and S56, Supporting Information) were used to construct the electronic energy level diagrams shown in Figure 5e.

The preceding demonstrates that these holey 2D nanostructures offer the dual advantages of rapid charge-carrier diffusion and significant reduction in the E_g from 3.36[29] to 2.89 eV. Further, there is the potential to leverage the effects of midgap trapping states (Figure 5c) associated with the presence of $V_O^{\bullet\bullet}$ and $V_{Ce}^{''''}$, although the positions of the corresponding energy levels do not appear to have been determined. Critically, Figure 5e demonstrates that the photocatalytic capacity for specific chemical reactions can be engineered by modification of the electronic band structure through the creation of nanostructures, as reported previously.[30] For example, Figure 5e shows that the FCO nanostructure lowers the E_g to 2.50 eV and positions the conduction band (CB), dark green line, for CeO_{2-x} above that of Fe_2O_3/Fe_3O_4 but also above the $O_2/{}^{\bullet}O_2^-$ energy level. The reduction of the bandgap significantly increases light absorption and the new CB position of FCO, which is in the proximity of $O_2/{}^{\bullet}O_2^-$, enhances the formation of reactive oxygen species (ROS) by enabling electron transfer from CeO_{2-x} to Fe_2O_3/Fe_3O_4. The VB and CB band alignments also suggest that charge transfer of both electrons and holes would be toward Fe_2O_3/Fe_3O_4, hence enhancing charge recombination. However, reduced electron/hole recombination of the mixed 0D/2D heterostructures relative to the CeO_{2-x} nanosheet was confirmed by PL spectroscopy (Figure S57, Supporting Information). These data suggest that charge transfer is dominated owing to short diffusion pathways in the nanosheets, rather than electron/hole recombinations.

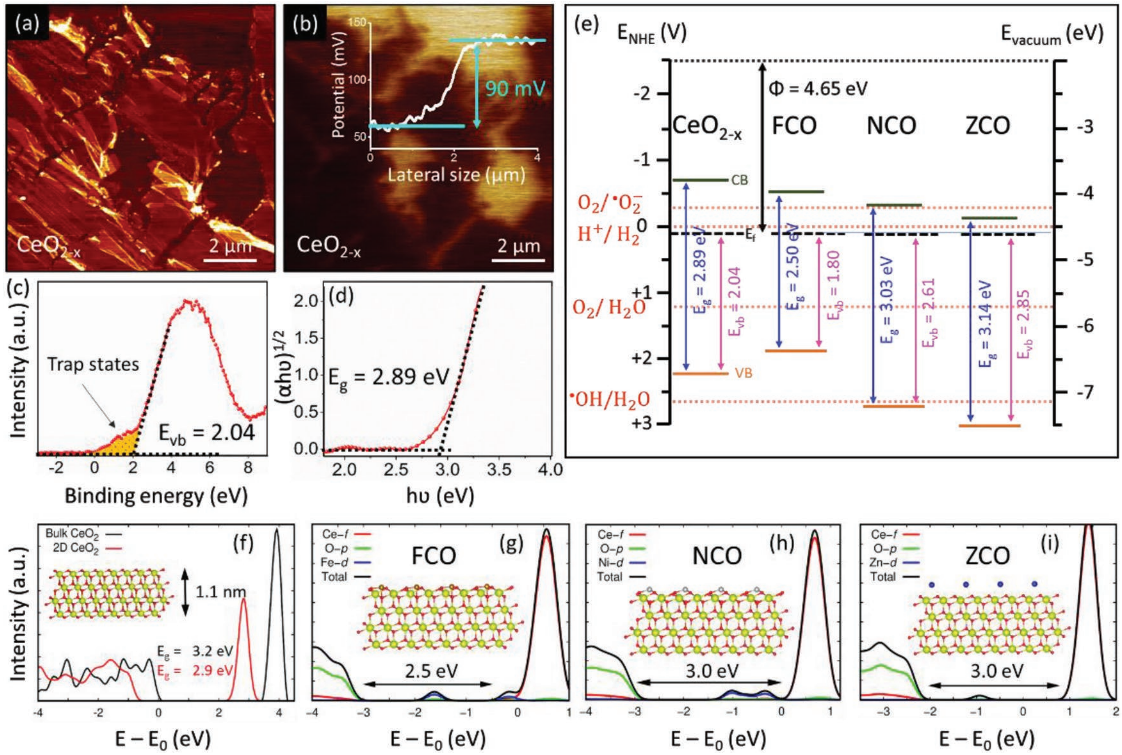

Figure 5. Band structure characterization of CeO_{2-x} and 0D/2D heterostructures. a) Topography of CeO_{2-x} holey nanosheet. b) Contact potential difference measured by KPFM of CeO_{2-x} holey nanosheet. c) XPS valence band plot for CeO_{2-x} holey nanosheet. d) Tauc plot from UV–vis spectrophotometry data for CeO_{2-x} holey nanosheet (Tauc plot model $(\alpha h\upsilon) = A(h\upsilon - E_g)^2$ applied, where A and α are absorption and absorption coefficient, respectively; $h\upsilon$ is photon energy; and E_g is optical indirect bandgap). e) Electronic energy level diagram for CeO_{2-x} holey nanosheet and 0D/2D heterostructures. f) First-principle DFT computations of electronic densities of states and bandgaps of CeO_2 nanosheets and bulk CeO_2. g–i) First-principle DFT computations of electronic densities of states and bandgaps of 0D/2D heterostructures.

XPS analyses (Figure S55, Supporting Information) of the NCO and ZCO nanostructure also showed the formation of trapping states. Although the bandgaps of NCO and ZCO were increased (Figure 5e), the CB in NCO and the VB in both NCO and ZCO are positioned appropriately to catalyze the $O_2/{}^{\bullet}O_2^-$ and ${}^{\bullet}OH/H_2O$ reactions, respectively, thereby enhancing the respective ROS formation. Further, both the VB and CB decreased relative to those for CeO_{2-x}, indicating that charge separation would be improved by electron diffusion to the TMO and hole diffusion to the CeO_{2-x}.

First-principle calculations based on density functional theory (DFT) were performed to characterize further the differences in electronic band structures between CeO_2 nanosheets, bulk CeO_2, and 0D/2D heterostructures. Figure 5f shows that the bandgap of the CeO_2 nanosheets is reduced by ≈10% relative to that of bulk CeO_2, which is in excellent agreement with the experimental result (Figure 5d). Upon adsorption of transition metal ions, noticeable variations in the band structure of the CeO_2 nanosheets are observed in the form of new electronic states appearing in the bandgaps (Figure 5g–i) and, in one case, the bottom of the CB (Figure 5g); the bandgaps are in good agreement with the experimental data (Figure 5e). The origins of such band structure differences are supported by differences in computed transition metal adsorption energies, which are −10.8 eV (Fe), −3.8 eV (Ni), and −0.1 eV (Zn). Larger charge transfers typically are correlated with more favorable adsorption energies.[31] Variations in electrostatic conditions result from significant differences in the amounts of charge that the transition metal ions transfer to the nanosheets (≈2 e^- per Fe ion, ≈1 e^- per Ni, and ≈0 e^- per Zn). These variations suggest a wide range of potential band tuning through the formation of 0D/2D heterostructures using different ions.[32,33]

Finally, the effects of band engineering on the photocatalytic performance were studied by photodegradation of methylene blue dye, as a standard for organic phase decomposition by ROS,[34] through 100 mW cm^{-2} of irradiance at AM 1.5 G solar illumination. While the holey CeO_{2-x} nanosheet exhibits a high dye degradation extent of 85% after 2 h (Figure S58, Supporting Information), the kinetics of the reaction reveals a rate constant (k) as high as 0.024 min^{-1}. The 0D/2D heterostructures performed even better, with FCO, NCO, and ZCO reaching extents of 100%, 94%, and 90%, respectively, after 2 h, showing high performance compared to the recent reports (Table S8, Supporting Information). The high stability of the samples was confirmed after multiple repeats of the photocatalytic tests. Figure S59 in the Supporting Information, shows that neither the nanostructure (SEM, TEM) nor mineralogy (Raman) was altered by stirring and following catalytic testing under solar irradiation. Further, the superiority in the performance of 0D/2D nanostructure, relative to the 0D/0D nanostructure, was investigated. Details of the results are provided in Table S9 in the Supporting information.

In summary, the present work represents a versatile metal-based coordination strategy to fabricate stratified structures. They are readily exfoliated in aqueous solution at room temperature into extremely thin holey nanosheets of MOs with advanced levels of functionalities for a wide range of energy and heterocatalysis applications. The unique behavior of these nanosheets originates from their holey architecture, minimizing the diffusion distance for charge carriers while maximizing the accessibility of active sites for catalytic reactions and/or charge storage. The band structure of the sheets could also be tuned during the process. Holey nanosheets of 2D nature can be used as a template to fabricate mixed 0D/2D heterostructures with transition metal components and beyond that can lead to promising routes for optimizing photocatalysts at the nanoscale regimes by tailoring their electronics through rearrangement of band positions.

Experimental Section

A detailed description of fabrication processes, mechanisms, characterizations, computational studies, and additional analysis can be found in the Supporting Information.

Supporting Information

Supporting Information is available from the Wiley Online Library or from the author.

Acknowledgements

This work has been supported by the Australian Research Council (DP170104130). The authors are grateful for access to the characterization facilities provided by the Mark Wainwright Analytical Centre, UNSW Sydney and beam time at the Wombat beamline of the Australian Nuclear Science and Technology Organisation (ANSTO). S.S.M. is pleased to acknowledge UPA and RTP scholarship support from UNSW Sydney. E.A. acknowledges the financial support (JSPS KAKENHI Grant Number: 18F18064) provided by the Japan Society for the Promotion of Science. M.C.S. and J.A. acknowledges funding from Generalitat de Catalunya 2017 SGR 327 and the Spanish MINECO project ENE2017-85087-C3. ICN2 is supported by the Severo Ochoa program from the Spanish MINECO (Grant No. SEV-2017-0706) and is funded by the CERCA Programme/Generalitat de Catalunya. M.C.S. has received funding from the European Union's Horizon 2020 research and innovation programme under the Marie Skłodowska-Curie grant agreement No. 754510 (PROBIST) and the Severo Ochoa programme. M.H. acknowledges support from the German Research Society under grant no. HI 1867/1-1. The authors thank J Design Solutions for providing the image for the table of contents.

Conflict of Interest

The authors declare no conflict of interest.

Author Contributions

S.S.M. designed the project; undertook the majority of syntheses and characterization, thermodynamic calculations, and data analyses; prepared the initial draft of the manuscript; and worked on all subsequent drafts of the manuscript. E.A. conducted large scale fabrication of CeO_{2-x} nanosheets and corresponding imaging; undertook TEM characterizations; contributed to crystallographic characterization, simulation, and data analysis of the Ce-CP; and worked on all drafts of the manuscript. R.P. undertook the syntheses of the Zr-CPs and Ti-CPs; their characterization; and commented on final version of the manuscript. M.H.N.A. conducted ab initio molecular dynamics simulation and related structural analysis. M.H. undertook neutron and X-ray structural characterization and related Rietveld analyses. Y.Y. conducted AFM and KPFM measurements. X.L. undertook photoluminescence measurement. M.B.G. conducted EDS imaging of heterojunction nanostructures. K.K.Z. assisted with the characterization and data analyses and commented on the final versions of the manuscript. R.M. undertook zeta potential measurements. C.C. undertook the DFT calculations and wrote the relevant text. R.S. undertook EPR measurements and analysis. G.B. undertook bandgap measurements. S.B. assisted in XRD measurement and analysis of the Ce-CP structure. M.C.S. and J.A. contributed to the EELS and HAADF imaging and commented on the final versions of the manuscript. S.L. and Y.X. contributed to the TEM imaging. H.A. assisted with the catalysis characterizations and commented on the final version of the manuscript. J.S. undertook BET tests. P.K. contributed to the data analyses and revised all drafts of the manuscript. C.C.S. worked on all drafts of the manuscript and supervised the overall project.

Keywords

2D materials, band alignment, heterostructures, holey nanosheets, metal-based coordination polymers

Received: August 16, 2019
Revised: October 8, 2019
Published online:

[1] L. Peng, Z. Fang, Y. Zhu, C. Yan, G. Yu, *Adv. Energy Mater.* **2018**, *8*, 1702179.
[2] K. Adpakpang, S. M. Oh, D. A. Agyeman, X. Jin, N. Jarulertwathana, I. Y. Kim, T. Sarakonsri, Y.-M. Kang, S.-J. Hwang, *Adv. Funct. Mater.* **2018**, *28*, 1707106.
[3] M. Qin, S. Li, Y. Zhao, C.-Y. Lao, Z. Zhang, L. Liu, F. Fang, H. Wu, B. Jia, Z. Liu, W. Wang, Y. Liu, X. Qu, *Adv. Energy Mater.* **2019**, *9*, 1803060.
[4] J. Guo, Y. Cao, R. Shi, G. I. N. Waterhouse, L.-Z. Wu, C.-H. Tung, T. Zhang, *Angew. Chem., Int. Ed.* **2019**, *58*, 8443.
[5] a) Y. Xu, Z. Lin, X. Zhong, X. Huang, N. O. Weiss, Y. Huang, X. Duan, *Nat. Commun.* **2014**, *5*, 4554; b) X. Zhao, C. M. Hayner, M. C. Kung, H. H. Kung, *ACS Nano* **2011**, *5*, 8739.
[6] a) P. Sennu, M. Christy, V. Aravindan, Y.-G. Lee, K. S. Nahm, Y.-S. Lee, *Chem. Mater.* **2015**, *27*, 5726; b) Y. Dong, W. Shi, P. Lu, J. Qin, S. Zheng, B. Zhang, X. Bao, Z.S. Wu, *J. Mater. Chem. A* **2018**, *6*, 14324.
[7] Z. Fang, L. Peng, H. Lv, Y. Zhu, C. Yan, S. Wang, P. Kalyani, X. Wu, G. Yu, *ACS Nano* **2017**, *11*, 9550.
[8] a) Z. Fang, L. Peng, Y. Qian, X. Zhang, Y. Xie, J. J. Cha, G. Yu, *J. Am. Chem. Soc.* **2018**, *140*, 5241; b) K. Xiang, Z. Xu, T. Qu, Z. Tian, Y. Zhang, Y. Wang, M. Xie, X. Guo, W. Ding, X. Guo, *Chem. Commun.* **2017**, *53*, 12410; c) L. Peng, P. Xiong, L. Ma, Y. Yuan, Y. Zhu, D. Chen, X. Luo, J. Lu, K. Amine, G. Yu, *Nat. Commun.* **2017**, *8*, 15139.
[9] a) D. Channei, S. Phanichphant, A. Nakaruk, S. S. Mofarah, P. Koshy, C. C. Sorrell, *Catalysts* **2017**, *7*, 45; b) S. S. Mofarah, E. Adabifiroozjaei, Y. Yao, P. Koshy, S. Lim, R. Webster, X. Liu,

R. Khayyam Nekouei, C. Cazorla, Z. Liu, Y. Wang, N. Lambropoulos, C. C. Sorrell, *Nat. Commun.* **2019**, *10*, 2594.
[10] H. Hojo, T. Mizoguchi, H. Ohta, S. D. Findlay, N. Shibata, T. Yamamoto, Y. Ikuhara, *Nano Lett.* **2010**, *10*, 4668.
[11] B. Feng, I. Sugiyama, H. Hojo, H. Ohta, N. Shibata, Y. Ikuhara, *Sci. Rep.* **2016**, *6*, 20288.
[12] Y. Lin, Z. Wu, J. Wen, K. R. Poeppelmeier, L. D. Marks, *Nano Lett.* **2014**, *14*, 191.
[13] B. Huang, R. Gillen, J. Robertson, *J. Phys. Chem. C* **2014**, *118*, 24248.
[14] a) F. Zhang, P. Wang, J. Koberstein, S. Khalid, S.-W. Chan, *Surf. Sci.* **2004**, *563*, 74; b) C. M. Sims, R. A. Maier, A. C. Johnston-Peck, J. M. Gorham, V. A. Hackley, B. C. Nelson, *Nanotechnology* **2019**, *30*, 085703.
[15] V. Stetsovych, F. Pagliuca, F. Dvorak, T. Duchon, M. Vorokhta, M. Aulicka, J. Lachnitt, S. Schernich, I. Matolinova, K. Veltruska, T. Skala, D. Mazur, J. Myslivecek, J. Libuda, V. Matolin, *J. Phys. Chem. Lett.* **2013**, *4*, 866.
[16] a) R. Mehmood, X. Wang, P. Koshy, J. L. Yang, C. C. Sorrell, *CrystEngComm* **2018**, *20*, 1536; b) R. Mehmood, S. S. Mofarah, W. F. Chen, P. Koshy, C. C. Sorrell, *Inorg. Chem.* **2019**, *58*, 6016.
[17] Springer-Verlag Berlin Heidelberg & Material Phases Data System (MPDS), Switzerland & National Institute for Materials Science (NIMS), Japan.
[18] D. A. H. Hanaor, C. C. Sorrell, *J. Mater. Sci.* **2011**, *46*, 855.
[19] S. Zinatloo-Ajabshir, M. Salavati-Niasari, *J. Mater. Sci.: Mater. Electron.* **2016**, *27*, 3918.
[20] Y. Zhao, G. I. N. Waterhouse, G. Chen, X. Xiong, L.-Z. Wu, C.-H. Tung, T. Zhang, *Chem. Soc. Rev.* **2019**, *48*, 1972.
[21] C. C. Sorrell, H. Taib, T. C. Palmer, F. Peng, Z. M. Xia, M. Wei, *Biological and Biomedical Coatings Handbook: Processing and Characterization* (Ed: S. Zhang), CRC Press-Taylor & Francis Group, Boca Raton, FL, USA **2011**, p. 81.
[22] a) R. S. Datta, J. Z. Ou, M. Mohiuddin, B. J. Carey, B. Y. Zhang, H. Khan, N. Syed, A. Zavabeti, F. Haque, T. Daeneke, K. Kalantar-zadeh, *Nano Energy* **2018**, *49*, 237; b) M. R. D. Bomio, R. L. Tranquilin, F. V. Motta, C. A. Paskocimas, R. M. Nascimento, L. Gracia, J. Andres, E. Longo, *J. Phys. Chem. C* **2013**, *117*, 21382.
[23] D. Jariwala, T. J. Marks, M. C. Hersam, *Nat. Mater.* **2017**, *16*, 170.
[24] J. M. López, A. L. Gilbank, T. García, B. Solsona, S. Agouram, L. Torrente-Murciano, *Appl. Catal., B* **2015**, *174–175*, 403.
[25] a) A. M. Jubb, H. C. Allen, *ACS Appl. Mater. Interfaces* **2010**, *2*, 2804; b) T. George, A. K. Dutta, M. S. Islam, V. Leichner, J. Kirtley, H. Eilers, *Proc. SPIE* **2018**, *10639*, 558.
[26] P. Ravikumar, B. Kisan, A. Perumal, *AIP Adv.* **2015**, *5*, 087116.
[27] S. J. Chen, Y. C. Liu, C. L. Shao, R. Mu, Y. M. Lu, J. Y. Zhang, D. Z. Shen, X. W. Fan, *Adv. Mater.* **2005**, *17*, 586.
[28] M. B. Ghasemian, M. Mayyas, S. A. Idrus-Saidi, M. A. Jamal, J. Yang, S. S. Mofarah, E. Adabifiroozjaei, J. Tang, N. Syed, A. P. O'Mullane, T. Daeneke, K. Kalantar-Zadeh, *Adv. Funct. Mater.* **2019**, *29*, 1901649.
[29] M. M. Khan, S. A. Ansari, D. Pradhan, D. H. Han, J. Lee, M. H. Cho, *Ind. Eng. Chem. Res.* **2014**, *53*, 9754.
[30] P. Liu, B. Xiang, *Sci. Bull.* **2017**, *62*, 1148.
[31] C. Cazorla, S. A. Shevlin, Z. X. Guo, *Phys. Rev. B* **2010**, *82*, 155454.
[32] Q. Sun, Z. Li, D. J. Searles, Y. Chen, G. M. Lu, A. Du, *J. Am. Chem. Soc.* **2013**, *135*, 8246.
[33] X. Tan, H. A. Tahini, S. C. Smith, *Energy Storage Mater.* **2017**, *8*, 169.
[34] a) S. A. Idrus-Saidi, J. Tang, M. B. Ghasemian, J. Yang, J. Han, N. Syed, T. Daeneke, R. Abbasi, P. Koshy, A. P. O'Mullane, K. Kalantar-Zadeh, *J. Mater. Chem. A* **2019**, *7*, 17876; b) W. F. Chen, S. S. Mofarah, D. A. H. Hanaor, P. Koshy, H. K. Chen, Y. Jiang, C. C. Sorrell, *Inorg. Chem.* **2018**, *57*, 7279; c) S. Das, A. Samanta, S. Jana, *ACS Sustainable Chem. Eng.* **2017**, *5*, 9086.